Search for Evidence of Cosmic Ray Acceleration by Supernova Remnant Kes 41 Using the *Fermi* LAT

by

Timothy Robert Joubert

Submitted to the Department of Physics
in partial fulfillment of the requirements for the degree of

Bachelor of Science in Physics

at the

MASSACHUSETTS INSTITUTE OF TECHNOLOGY

June 2013

Author .....
Department of Physics
May 10, 2013

Certified by .....
Enectali Figueroa-Feliciano
Assistant Professor, Department of Physics
Thesis Supervisor

Accepted by .....
Nergis Mavalvala
Senior Thesis Coordinator, Department of Physics

Search for Evidence of Cosmic Ray Acceleration by Supernova Remnant Kes 41 Using the *Fermi* LAT

by

Timothy Robert Joubert

Submitted to the Department of Physics
on May 10, 2013, in partial fulfillment of the
requirements for the degree of
Bachelor of Science in Physics

Abstract

The analysis presented in this paper incorporated photon events received during the full run time of the Fermi Gamma Space Telescope (FGST) Large Area Telescope (LAT) to date. By studying the γ emission of the supernova remnant (SNR) Kes 41 for the energy range $\sim$ 200MeV-200GeV, the γ-ray morphology and spectrum were measured. These measurements required the use of reduced log likelihood statistics mediated by the Fermi Science Tools toolkit, developed for LAT analysis. The spatial analysis of the γ-ray emission was measured at 5σ for the area within and around the contours established during radio measurements [25]. It also resembles Kes 41's observed, centrally bright, X-ray emission [18, 25]. Spectral analysis was also carried out and the resulting γ-ray spectrum was successfully fit to a power-law model of emission consistent with π^0-decay, a form of non-thermal emission caused by cosmic ray acceleration. An overall approximation of the γ-ray luminosity was then measured as $L_\gamma = 1.94 \times 10^{35}$ erg/s using a measure of the total γ-ray flux. A calculation also measured the particle density associated with material interacting with Kes 41 emission as $n = 0.15$ particles/cm^{-3}. This value resembles that from other calculations involving SNR-Molecular cloud interaction [22]. This interaction serves to constrain γ-ray emission to the π^0-decay channel, so evidence of a similar density value may be evidence that the significant γ-ray emission observed, was due to the acceleration of cosmic rays.

Thesis Supervisor: Enectali Figueroa-Feliciano
Title: Assistant Professor, Department of Physics

Acknowledgments

To begin I would like to acknowledge my thesis supervisor Professor Enectali Figeuroa-Feliciano for allowing me the opportunity to work this past year within the Kavli Institute for Astrophysics. This field has been my passion for a long time and I yearned for the opportunity to really sink my teeth into good research. This project was everything I had been waiting for. I cannot thank him enough for the chance he gave me.

I would also like to acknowledge Daniel Castro whom I worked with closely throughout this project. His tutoring and patient instruction aided not only in my technical and computing competency, but truly ingrained in me a genuine understanding of the amazing and complex physical processes involved in the work presented in this paper. Without Daniel's help I would never have been able to finish this project and would have gotten far less out of this whole process. This research has changed my goals as a physicist and bolstered my resolve to pursue further research in astrophysics.

I am also very grateful to Professor Christoph Paus and Professor Markus Klute who first granted me entrance into the world of High-Energy physics my sophomore Spring. The technical knowledge I gained from my experiences with the CMS collaboration at MIT opened the doors that allowed me to pursue the field I most enjoy. I am truly in debt to both men for the opportunities they gave me to grow within the physics community. I of course would also like to thanks Max Goncharov for his careful guidance and warm demeanor, which made learning a difficult process that much easier.

I would like to also acknowledge Jeff Livas for my first exposure to professional astrophysics which began during my time at the Goddard Space Flight Center. Under Jeff's tutelage I was able to complete more work in one month then I have any other time in my life and was able to do it with a smile. That IAP was an amazing growing experience for me as an individual and especially as an experimental physicist. I would really like to thank him for his wonderful mentorship.

No MIT physics major can ever speak on his undergraduate career without the mention of Junior Lab. Luckily I ended up with both an excellent partner and an engaged professor. Despite the difficulty of the course, Professor David Litster fostered in me a practiced experimental approach and scientific tact. Though there were set backs early on, I grew as a physicist to a point where I am confident in my scientific writing ability and laboratory techniques. These are skills that I have taken with me to every new project and that have already come to my aid. I am excited to use them further and could not thank Professor Litster enough for his teaching and subsequent support.

My undergraduate career in physics has been an amazing ride with many highs and lows. Throughout it I have tried to manage the rigors of an MIT education and completing the Air Force ROTC Officer training program. On top of these responsibilities I have also played varsity soccer all four years and been a brother of the ΦΣK fraternity. All of these pulls on my time and attention would have been unbearable if it were not for the support of friends and colleagues I have made in these organizations.

I would like to acknowledge Gustaf Downs for his help throughout our physics education and my physics mentors, Javier Duarte and Antony Speranza for setting a high bar for me to meet. I also would like to acknowledge Ben Lewis, Thomas Fronk, Cameron McCord, my other soccer teammates, Ray Tilden, Jason Hoch and the rest of my fraternity. They have all been a constant rock of friendship and support. Thanks also to Alexis Giguere for giving me an unconditional friendship that started and grew through the rigors of Jlab, will certainly not be limited to our time at MIT.

To finish, I would like to dedicate this thesis, the culmination of my education and efforts devoted to physics this past four years, to my Mother Gail, Father Pierre and my Grandfather Eugene Stirling. Without all of your support I would have simply stopped on several occasions, especially in the beginning years. I owe you all everything and I cannot thank you enough for the life and opportunities you have afforded me so far. You were always my inspiration. And of course thanks to my twin brother Matt for being a constant friend throughout my life.

Contents

List of Figures

THIS PAGE INTENTIONALLY LEFT BLANK

Chapter 1

Introduction

Products of cosmic ray acceleration were first discovered by Victor Hess in 1912 [23]. Following this discover, cosmic ray astronomy was pioneered by Bruno Rossi, a professor at MIT at the time, in the 1930s and initially relied on the sea level detection and study of cosmic ray muons [28]. These muons are produced due to a series of successive interactions between particles of Earth's atmosphere and incoming primary, hadronic cosmic rays. These interactions produce both electromagnetic and hadronic showers of particles within the atmosphere including extremely energetic muons. These muons have been detected at energies corresponding to primary cosmic ray energies on the order of 10^{16}- 10^{21} eV. Until recently these muons have been the only outlet for particle physicists to observe the products of such extraordinarily energetic collisions.

Despite the high energy of the resulting particles from these interactions, there are many difficulties and sources of uncertainty involved with ground-based detection. These uncertainties stem from the turbulence and unpredictability of half of the interacting medium in these interactions, the Earth's atmosphere. The dynamic atmosphere is the source of numerous background production mechanisms caused by physical processes unrelated to the muon production. This has required many experiments to incorporate an excessive amount of shielding that restricts the energies of particles reaching the detector surfaces and significantly limits their angular resolution [1, 21]. The Fermi Gamma Ray Space Telescope (FGST) however is now

providing scientists with an alternative to the often noisy and uncertain ground based measurements by avoiding Earth's atmosphere entirely, and detecting cosmic ray particles from low-Earth orbit.

A main focus of Cosmic Ray astronomers is determining the origins of these Cosmic Ray emissions. This has remained a mystery to astrophysicists since Rossi's first detections using a Geiger tube setup [28] . Since Rossi's time, methods of detection have improved greatly and multiple competing theories have been developed attempting to describe cosmic ray acceleration. This paper will attempt to provide evidence of cosmic ray acceleration due to shock acceleration during supernova. This will be done by studying localized high energy, γ-ray emission from a region surrounding the center of a proposed point source, supernova remnant G337.8-0.1, also known as Kes 41. The rest of this chapter will describe the current theorized method of shock acceleration which will be followed by a description of the origin and emission of supernova remnants in Chapter 2. Then the paper will discuss the radio and X-ray emission of the source of interest, Kes 41 including comments on its morphology and proximity to a source of maser emission in Chapter 3. Following this will be a discussion of the apparatus used to conduct this investigation, the FGST Large Area Telescope in Chapter 4, and then an in depth discussion of the experimental methods in Chapter 5. The results of this study are then described at length in Chapter 6, including Kes 41's γ-ray morphology and spectrum. This is then followed by a brief summary of the analysis in Chapter 7.

1.1 Cosmic Rays and Acceleration Mechanisms

Interstellar space is composed of neutral and ionized gas, dust, photons, neutrinos and high-energy charged particles. These high-energy particles exist typically in the form of cosmic rays. These extremely energetic and highly relativistic streams of charged particles are composed of roughly 90% protons and 9% helium nuclei with smaller contributions from electrons ($\sim$ 1%) and heavier nuclei [11]. The source of these streams of high energy particles has yet to be identified but many astrophysicists

believe that production may be tied to supernova remnants (SNRs) [11]. Blandford suggests that expanding shock waves from these massive stellar explosions accelerate Cosmic Ray particles through the diffusive shock acceleration process (DSA), also known as first-order Fermi acceleration [11]. Fermi describes this acceleration as the result of charged particles colliding against irregularities of magnetic fields as well as against the highly heterogeneous interstellar medium [20]. Due to the massively ener-

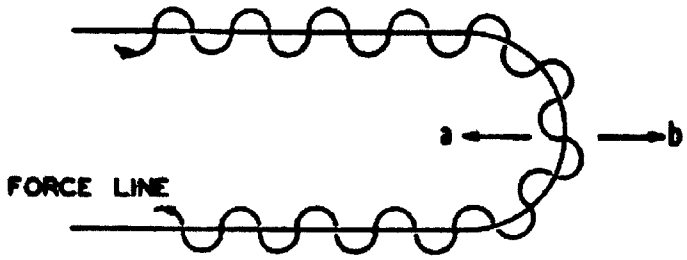

Figure 1-1: Trajectory of orbiting charged particle about a magnetic field line [20]. If the field line is moving in the direction of a, the particle is accelerated through collision with the high intensity region

getic ionizing processes of supernovae, magnetic fields may be created with complex dynamic characteristics. These fields cause charged particles to orbit along the "lines of force" [20] with a characteristic angle of orbit with respect to the field. This angle is described as the angular difference between the direction of the field line and the direction of the velocity of the particle, as shown in Figure 1-1. If an area of high field intensity moves toward the orbiting cosmic ray particle, a collision will occur that changes the angle of orbit to its maximum such that the particle experiences a large addition to its velocity given by Equation (1.1). This is due to the fact that $\sin^2\alpha/\mathrm{H} \approx$ constant, where α is the orbit angle and H is the local field intensity.

$$\frac{w'}{w} = \frac{1 + 2B\beta\cos(\alpha) + B^2}{1 - B^2} \tag{1.1}$$

In Equation (1.1), β can be taken as the particle's velocity while B is the velocity of the moving area of high field intensity.

Other proposed sources of this type of acceleration include pulsar wind nebulae such as the Crab Nebula, high-mass binary sources such as Cygnus X-3 [30], and blazar

active galactic nuclei jets (AGNs) [7]. Within the interstellar medium (ISM) further acceleration occurs through processes including Bremsstrahlung, inverse Compton scattering and nucleon scattering [30]. All of these sources result in the emission of a diffuse cosmic ray background [11,30]. We will now take a closer look on how particle shock acceleration may occur due to stellar explosion as well as the corresponding photon emission mechanisms.

Chapter 2

Supernova Remnant Formation, Morphology and Emission

Supernovae result from enormous explosions of stars caused by either core collapse or thermonuclear reactions resulting from explosive nuclear burning. A stable stellar system of mass $M \gtrsim M_{\odot}$ steadily fuses Hydrogen nuclei and uses the resulting energy to resist the crushing forces from its own gravity, thereby maintaining an equilibrium of interior forces. As the Hydrogen concentration decreases, the gravitational energy begins to compact the interior of the star, in turn heating up the core. This additional energy prompts the fusion of Helium elements, forming a denser core of higher atomic number. This process continues until finally the gravitational forces overcome the results of the fusion processes and the core reaches the Chandrasekhar mass, $M \sim 1.44M_{\odot}$. At this point, the core has reached the condition for when it can be supported by electron degeneracy pressure [14]. This results in a sudden collapse of the stellar core prompting a rapid shedding of the outer atmospheres, driven by an enormous magnetohydrodynamic shock wave [33]. This is defined as a Type II core collapse supernova.

For truly massive stars, $M \gtrsim 4M_{\odot} - 8M_{\odot}$, the fusion process will continue as heavier element groups fuse until silicon fuses to form ^{56}Fe. Because ^{56}Fe has the most strongly bound nuclei, more energy must be absorbed than is actually released by fusing two nuclei. This causes a rapid core collapse resulting in an enormous

shock wave of liberated gravitational energy on the order of $\gtrsim 10^{51}$ erg that ejects the surrounding atmospheres. For such massive stars the end result may be either a neutron star, that is a star supported by neutron degeneracy pressure, or even a black hole [14, 27, 33].

The second type of supernova, Type Ia, occurs when stellar objects, generally thought to be white dwarfs, begin to acquire matter from surrounding astrophysical bodies. The most predictable source of this matter exchange is from white dwarf binary systems where the white dwarf siphons off material, believed to be mainly Hydrogen and Helium, from the outer atmospheres of its companion star. As the white dwarf adds to its mass, it reaches a point where its mass becomes greater than the Chandrasekhar mass, $M \sim 1.44 M_{\odot}$ [14]. This prompts further core collapse by itself but this also simultaneously increases the core temperature to a point where Carbon can begin nuclear fusion before the collapse fully initiates. This causes a runaway nuclear fusion reaction which release enough energy to completely unbind the star causing a thermonuclear explosion [33]. Because Type Ia supernovae are the result of the explosion of stars of similar mass, white dwarfs, these supernovae have very similar properties including a characteristic luminosity. Astronomers use these so called "standard candles" to more accurately estimate the red shift of nearby astrophysical objects.

Supernova explosions are often extremely luminous, emitting broadband radiation across a large range of energy. Occasionally these stellar explosion outshine their entire host galaxy and are visible with the naked eye. This includes the supernova SN1006 which occurred in the year 1006 AD and was observed and recorded by civilizations all over the world. The ejected circumstellar medium travels at velocities up to several thousands of kilometers per second, causing electromagnetic and plasma shock waves that interact with and rapidly heat surrounding interstellar material through collisionless interactions to temperatures on the order of millions of degrees Kelvin. The result of this expanding shock wave is a supernova remnant (SNR) which can extend for tens of parsecs and last for hundreds of thousands of years.

Such explosions typically result in the formation of visible shells, radiating at

radio wavelengths near their shock fronts. These SNRs are termed shell-type. When supernova result in the formation of a pulsar at the center of the shell, the energy lost from this rotating neutron star produces a "wind" relativistic charged particles. These particles emit γ-rays at GeV and TeV energies which appear as a cloud of high energy photons near the center of the SNR, and are classified as pulsar-wind nebula SNRs. This affect dominates the radio emission from the shock front creating a *center-filled* appearance of X-ray and γ-ray energy [27,33] The final classification is the composite SNR which has characteristics of both pulsar-wind nebula and shell SNRs. These can include either pulsar produced X-ray emission or high energy emission from plasma heated by the shock front. Both have shells emitting at radio wavelengths [27,33].

These supernova remnants provide a unique look into the composition of stars and even the chemical evolution of the universe. Both the spatial and spectral qualities of individual SNRs tell a great deal about the type of star and the influence of the resulting shock wave on the surrounding material. Through careful analysis of the broadband spectrum of supernovas we may understand the emission processes of supernovae and hopefully gain insight into problems including the nature of cosmic ray acceleration.

2.1 Thermal Emission

Following a supernova event, shock waves transform a majority of the kinetic energy into thermal energy. Heating is typically due to Coulomb interactions where the distance of closest approach, the impact parameter b, is given by

$$\frac{1}{2}\frac{m_1 m_2}{m_1 + m_2}\nu^2 = \frac{Z_1 Z_2 e^2}{b} \tag{2.1}$$

where m_1 and m_2 are the particle masses, $Z_1 e$ and $Z_2 e$ are the particles charges and ν is their relative velocity. This typically results in a collision time scale that is much slower than the expansion of SNRs. Therefore, the plasma heating due to the SNR shock waves must be the result of fluctuating electric and magnetic fields [33]. Also,

the collision density is thirteen orders of magnitude smaller than the range Coulomb collisions may occur. Due to the inherent low density of astrophysical shocks, this energy is exchanged with the surrounding material through collisionless processes instead of particle-particle interactions. This creates a broadband continuum spectrum due to bremsstrahlung emission and two-photon emission.

Bremsstrahlung emission is essentially derived from the Lorentz force of electromagnetism. As a particle moves into the field caused by another charged particle, it is decelerated by the force exerted on it. This deceleration results in the emission of radiation because of a second EM result, that accelerating charges emit radiation. For the case of a moving, low density, astrophysical plasma, which is the case of supernova shock waves, this type of radiation is termed free-free radiation. This refers to the fact that the charged particles involved are free both before and after the interaction. Bremsstrahlung radiation forms a continuum including photon energies ranging from radio wavelengths to X-ray emission. They provide the majority of the thermal continuum which is given as a Maxwellian emissivity distribution,

$$\epsilon_f \propto T^{-(1/2)} e^{-\frac{h\nu}{k_B T}} \tag{2.2}$$

where T is the electron temperature and $h\nu$ is the energy of the photon [33].

Another source of SNR thermal emission is line emission due to excited emission of materials, typically ions, within the SNR. This excitation is dominated by electron-ion collisions [33]. The photons emitted in these lines correspond to the separation in quantum energy levels of the ions themselves and are used to determine the composition of astrophysical objects including SNRs. For the case of very low density astrophysical plasmas, these ions can be assumed to begin in the ground state and both collisional de-excitation and further excitation can be ignored. The emission is characterized as line emission because its presence is seen in the form of a near delta-function rising from the emission spectrum from the thermal continuum emission.

Evidence for non-thermal emission, that is emission of photons not directly tied to

heating, has been noticed in several SNRs. Many SNR shells have a radio brightness that is much too high to be explained by interstellar electron compression and the resulting magnetic fields. The next four emission mechanisms fall under the category of non-thermal emission as they incorporate charged particles accelerated by the expanding supernova shock wave. Therefore, the emission from these non-thermal processes are theoretically the result of cosmic ray acceleration due to supernovae. Significant detection of photons at energies characteristic of these three processes will provide evidence that the proposed source, SNR Kes 41, does accelerate cosmic rays.

2.2 Synchrotron Radiation

A basic tenant of electromagnetism is that accelerated charges emit radiation. In the case of SNRs, we must consider electrons and positrons accelerated by shocks to relativistic speeds, called leptonic cosmic rays. These particles are constantly interacting with the complex electromagnetic environment. As the magnetic fields change and the relativistic electrons are manipulated by the fields, the electrons change direction as given by the Lorenz force. This change of direction is different than what was described for Bremsstrahlung because instead of the electrons interacting with other charged particles, these relativistic electrons are manipulated through collisionless processes, meaning they are influenced by the intense magnetic field lines themselves. Because of their high energies, these electrons can emit photons ranging from low frequency radio emission up to X-ray energies [33]. In fact nearly the entire range of radio emission from SNRs comes from the synchrotron process [27].

The majority of SNRs are radio sources because synchrotron emission typically occurs at energies corresponding to radio wavelengths with synchrotron X-ray emission given by electrons near the maximum energy of the relativistic electron distribution. Due to the dependence of this process on the magnetic field, we can see that the higher the magnetic field intensity, the higher the radio synchrotron flux. A relativistic electron radiates a continuous synchrotron spectrum of radiation with its

maximum emission occurring at the characteristic frequency,

$$\begin{aligned} \nu_{max} &= 1.82 \times 10^{18} B E^2 Hz \\ h\nu_{max} &= 19.3 \left(\frac{B}{10\mu G}\right) \left(\frac{E}{100TeV}\right)^2 keV \end{aligned} \tag{2.3}$$

For inside SNRs, the magnetic field, B typically ranges from $B = 10-500\mu G$, creating TeV electrons, resulting in photon emission energy spectrum extending into a few 10s of keV [27, 33].

Synchrotron radiation is one of three leptonic, non-thermal emission processes typically associated with SNRs. The term leptonic indicates that the emission is caused by the movement of leptons, specifically electrons. These electrons are also considered non-thermal because the synchrotron radiation is not due to their heating but rather their movement due to the DSA process, a non-thermal effect.

2.3 Non-Thermal Bremsstrahlung

As was explained in Section 2.1, thermal bremsstrahlung radiation results from electron deflection off of another charged particle. Non-thermal electrons also emit bremsstrahlung radiation but at even higher energies. The same shock acceleration processes that prompt synchrotron radiation at keV ranges also contributes MeV-GeV, and even TeV, bremsstrahlung photons [33]. An accelerated electron of non-relativistic to mildly relativistic energy, E, can emit photons of energy $E/3$. Therefore this range can emit X-ray radiation even for electrons of non-relativistic energies. This form of emission is not nearly so dominate as other TeV and GeV emission processes because of the low particle density of supernova shocks. It is most likely contained in a thin band of the shell of supernovae. It could however, offer astrophysicists some insight into the lower range of cosmic ray distributions [27].

2.4 Inverse Compton Scattering

A relativistic electron can also emit radiation independently of interactions with magnetic fields or other particles. Highly relativistic electrons can also upscatter low energy ambient photons to γ-ray energies through a process called inverse Compton scattering. For SNRs, this is an important mechanism for the production of MeV-GeV and TeV photons and depends on the absolute highest, most relativistic range of the electron distribution [27]. This high energy condition is necessary to produce high energy photons because scattering typically results in an increase of the photon momentum by a factor of $\sim 2\gamma^2$.

The most likely source of seed photons for this inverse Compton scattering process is the cosmic microwave background (CMB), [27]. The photon spectrum is therefore given by a blackbody distribution at a temperature of $T \simeq 2.73K$, expressed by Planck's law,

$$B_\nu(T) = \frac{2h\nu^3}{c^2} \frac{1}{e^{\frac{h\nu}{k_B T}} - 1} \tag{2.4}$$

This results in a roughly Maxwellian distribution of the resulting high energy photons, assuming the electron flux is mono energetic. As we can see, this process creates some of the most energetic photons. This production mechanism can sometimes be the largest producer of non-thermal emission from some SNRs. However, this is commonly rivaled by another non-thermal mechanism which is not leptonic but hadronic in nature.

2.5 π^0 Decay

We have just explored three emission mechanisms and their associated photon distributions caused by leptonic cosmic ray acceleration within supernova remnants. These three processes resulted from either the deflection of an electron through interactions with another charged particle, or with a magnetic field, or by the upscattering of ambient photons. While these processes all result in significant X-ray and γ-ray energy photon spectra, the commonly dominant production mechanism for γ-ray energy

photons is a hadronic process involving particle collisions. A hadronic process is simply one that results from hadronic cosmic ray acceleration through the DSA process, described in Section 1.1. Supernova may accelerate protons to enormous energies, and may even indirectly prompt their collision.

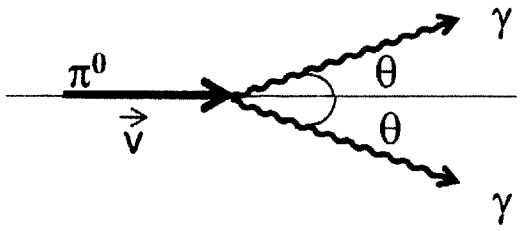

Figure 2-1: Diagram of neutral pion decay

Proton-proton collisions produce huge cascades of intermediate particles that then decay into even more particles, as described briefly in the Introduction. One of these intermediate particles is the neutral pion, π^0. As a result of the high energy collision that created them, an isotropic distribution of π^0's will follow a $\pi^0 \rightarrow \gamma + \gamma$ decay process and releases photons of γ-ray energies [27]. Despite the low cross section for proton collisions, the massive number of protons accelerated by the shock results in enough neutral pion-producing collisions, that π^0 decay is typically the dominant TeV γ-ray photon production channel. The spectral distribution, dN/dE of hadronic cosmic ray emission is typically modeled as a power law distribution with an exponential energy cut off, E_0,

$$\frac{dN}{dE} = aE^{-\Gamma}e^{\left(\frac{E}{E_0}\right)} \tag{2.5}$$

The interaction of cosmic ray protons with regions of high-density material promise a larger number of proton-proton interactions [16].

2.6 OH Masers

Interaction with surrounding material should result in more γ-ray production due to a higher density of material [16]. Evidence of gamma ray production for several SNRs

adjacent to molecular clouds (MC) has been observed [3, 16]. In fact they are among the most luminous GeV sources in the galaxy [22]. The connection between SNRs and MCs could potentially provide interesting knowledge on the physical characteristics of both. Typically stars develop in close proximity to their progenitor clouds of material. During the life of a star, they constantly influence these clouds [25]. Following supernova, the SNR continues to interact and by better understanding this interaction through study of the emission, advances may be made on topics including stellar evolution. Also, SNR-MC interaction help to constrain the source of γ-ray emission from SNRs to proton-proton collisions due to DSA [22]. This therefore allows better confidence in observations of cosmic ray acceleration.

Sources of stimulated spectral line emission were first discovered in 1963 by Weinbreb. This emission is typically at radio wavelength and has been empirically tied to the composition of MCs it has been observed near or within. This first source was located within Cassiopeia A, and had a 18-cm absorption line corresponding to a Hydroxyl, OH, absorption. The ground state of the Hydroxyl molecule has two main line emissions and two satellite lines. Of the satellite lines, 1720.530 MHz is the one of interest in this paper. This was first observed by Goss and Robinson in 1968 toward the SNRs W28 and W44 [25]. These SNRs became prototypes for SNRs interacting with molecular clouds [25].

OH maser emission has become the most commonly observed type of maser emission associated with SNR-MC interactions. Criteria for these interactions includes close agreement in both measured position of the OH (1720 MHz) maser and the SNR of interest, and also that the maser emission be observed interior to or at the radio continuum edges of the SNR [25]. Also, while detection of OH maser emission within an SNR is strong evidence of shock interaction with a molecular cloud the absence of maser emission does not mean there are not interactions. In this way maser emission can be used as a tool to locate SNR-MC interaction but is not the only one. Therefore, by finding SNRs in the vicinity of compact maser emission, astrophysicists can better predict the existence of proton-proton collisions [25].

The emission spectrum of supernova has been modified and improved following

observation of the broadband spectrum of individual SNRs. Figure 2-2 shows the observed emission spectra, and fitted theoretical models, for each emission channel of SNR G347.3-0.5. The gray curve can be interpreted as typical radio emission due to synchrotron radiation while the high energy end of the plot shows X-ray and γ-ray emission due to non-thermal Bremsstrahlung, inverse-Compton scattering, and neutral pion decay. This paper will perform a spectral analysis on Kes 41's high energy emission, corresponding to the γ-ray band seen in this plot.

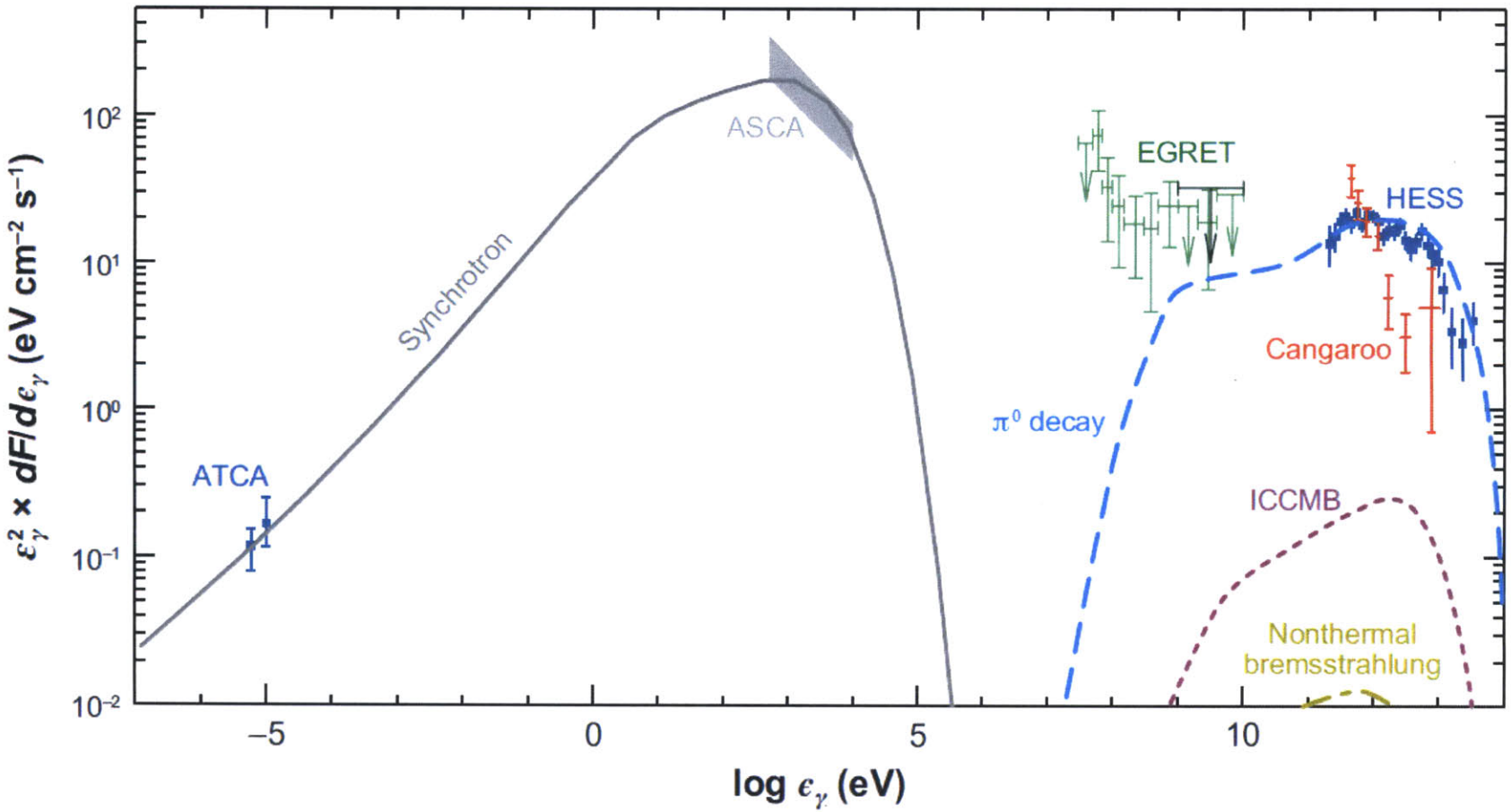

Figure 2-2: Model for the broadband spectrum of SNR G347.3-0.5 including gamma ray observations from the EGRET, HESS and Cangaroo experiments [10]

THIS PAGE INTENTIONALLY LEFT BLANK

Chapter 3

Kes 41

The focus of this investigation is the supernova remnant G337.8-0.1, also known as Kes 41. This remnant was chosen because of its proximity to an OH Maser emitter as well as the detection of thermal X-ray emission at its center, which indicate favorable circumstances for studying cosmic ray acceleration [18, 25]. As was described in Section 2.6, the presence of a nearby maser means that the SNR is interacting with more dense material, meaning that any significant γ-ray production will most likely be the result of the π^0-decay mechanism because of the increased likelihood of proton-proton collisions.

3.1 Radio Observations

Kes 41 was first detected in 1970 with the Molonglo telescope at 408 MHz and is reported in the Molongo Observatory Synthesis Telescope (MOST) catalog as a bright small-diameter SNR and distorted shell with a center at coordinates in right ascension and declination, (RA, Dec) = (249.75, -45.983333) [31]. This detection is shown in Figure 3-1a. Figure 3-1b shows the results of an additional radio observation made by Whiteoak and Green in 1996 which gives the most accurate image of the SNR's radio characteristics to date [32]. This is an 843 MHz continuum image which includes contours for 55, 140, 290, 380, 420, 470, 540, 630, 710 and 780 mJy beam^{-1}. From this image we can clearly describe Kes 41 as a distorted, shell-type SNR. This is

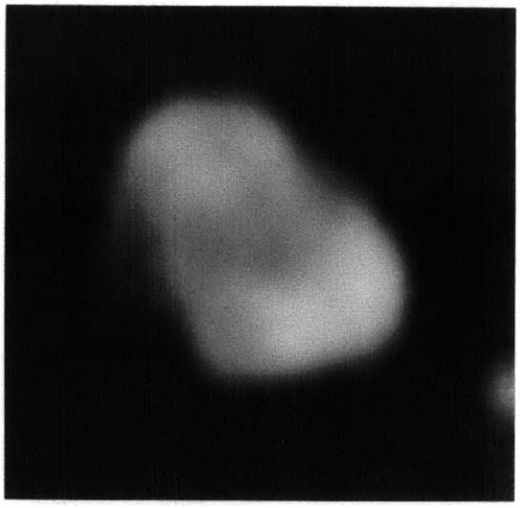

(a) 408 MHz image of Kes 41 following first observation in 1970 [31]

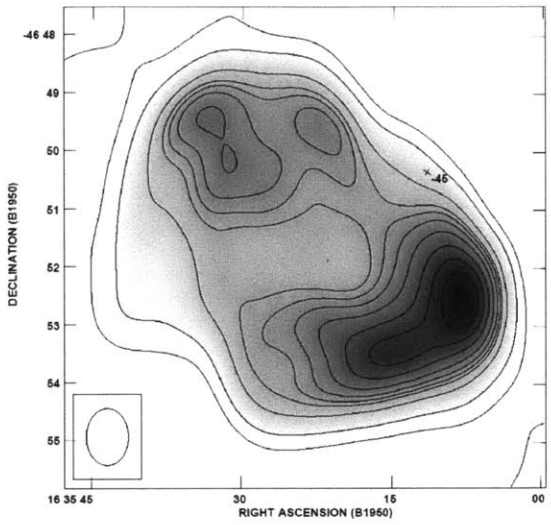

(b) Radio image and contours for 843 MHz observation of Kes 41 in 1996 and proximate maser emission given by the cross [25, 32]

Figure 3-1: Radio observations and contours for Kes 41

because the radio emission appears to come from the shock front and it does have a non-spherically symmetric morphology [18]. This emission appears particularly concentrated in two separate points indicated by darker colored portions in the figure. Koralesky also observed Kes 41's radio emission in 1998 and made a measure of its kinematic distance using the observation of OH-maser emission, marked in the image by the small cross [25]. This measure put Kes 41 a distance of 12.3 kpc and established that its $6' \times 9'$ size corresponds to an actual diameter of 15×20 pc [25]. Kes 41 therefore has all of the radio criteria to suggest its interaction with a molecular cloud. Also, this radio emission can be interpreted as the result of non-thermal, synchrotron radiation from accelerated high-energy electrons [18].

3.2 X-ray Emission

Astronomers have also made observations of X-ray emission from Kes 41. Figure 3-2 shows an X-ray image taken by Combi in 2008 using the XMM-*Newton* Observatory [18]. Several early attempts to detect Kes 41's X-ray emission failed due to lack of X-ray sensitivity of observing apparatuses. In this image, taken for the energy

range 0.5-10 keV, the radio contours from the MOST catalogue is superimposed in yellow [31].

There is a clear concentration of X-ray photons in the center of picture with a concentration toward the southwest "peak". This serves to characterize Kes 41 as centrally bright for X-rays with out indication of pulsar-wind nebula attributes. Combi's analysis included flux measurements for four different energy ranges. The range from 2-4 keV was measured to have a flux $F = 1.6 \times 10^{-13}$ erg s^{-1} cm^{-2}, corresponding to 58 % of the flux. This range includes hard X-rays, suggesting that observation of γ-ray energies is quite possible. This analysis also serves to restrict the source of X-ray emission to that dominated by thermal X-rays, labeling the SNR as a thermal composite remnant [18]. This restriction was made by Combi due to not only the apparent filled-center morphology, but also through his analysis of the SNRs spectral lines.

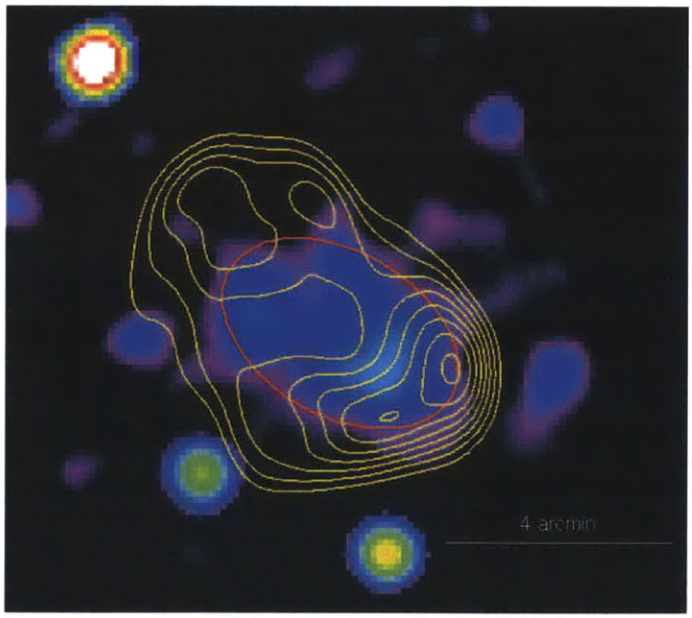

Figure 3-2: Image of X-ray emission from Kes41 taken by the XMM-*Newton* Observatory. Superimposed in yellow is the measured radio continuum from 1996. The morphology is clearly centrally bright and well contained within the radio contours [18]. The area of significant localized X-ray emission is contained by the red ellipse

Combi's spectral analysis analysis of the SNR was conducted using a similar method to what will be done during the analysis presented in this paper. By compar-

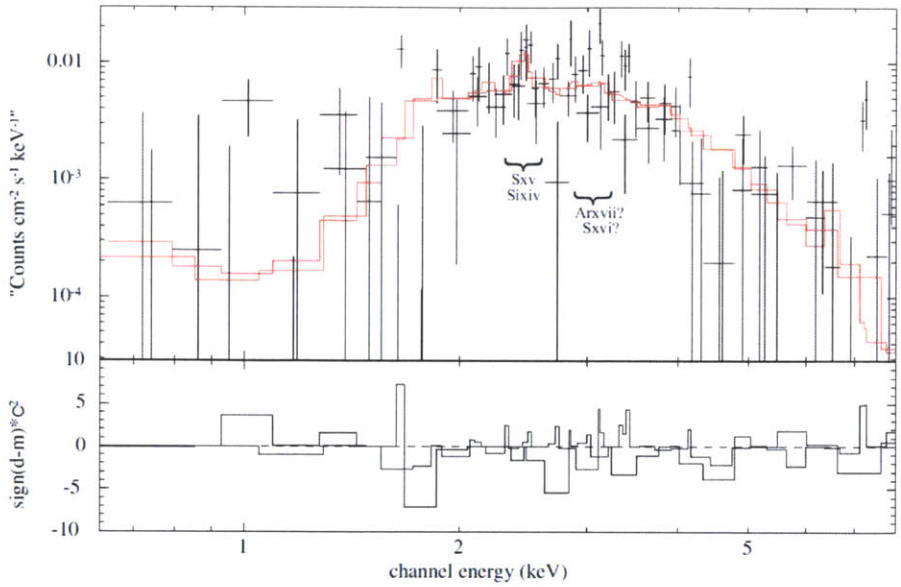

Figure 3-3: XMM-*Newton* spectrum for diffuse X-ray emission including the solid line of best fit based on χ^2 statistics, and plot of its corresponding residuals. The most intense spectral lines are given by the Sxv and Sixiv indicators [18]

ing predictions of a theoretical model to the actual data, a statistic was measured and reported. This resulted in the spectrum given by Figure 3-3. Here we have a plot of the data along with the best fit model, red line, derived using χ^2 statistics for several energy ranges [18]. These images and this spectrum give a strong point of comparison for future observations of Kes 41 at higher energies, such as the work presented in this paper. During analysis, both the radio contours and the X-ray image will be cross reference in order to validate the significance of γ- ray detection.

Chapter 4

Fermi Large Area Telescope

The data set that is used during this research comes from the FGST's Large Area Telescope (LAT) seen in Figure 4-1, and represents events collected from August 4, 2008 through March 8, 2013. The Fermi Gamma Ray Large Area Telescope can detect particles within an effective energy range ~30MeV - 300GeV. The LAT has a field of view of roughly 20% of the sky and is positioned in low Earth orbit. Starting in August 2008, the telescope entered a survey mode which saw the LAT observing the entire sky every two Earth orbits. This corresponds to a new picture of the gamma-ray sky every 3 hours. This is certainly a huge step forward in gamma-ray astronomy but is also very promising for the study of cosmic rays and their potential sources [9].

High energy γ-rays cannont be reflected or refracted as would be incorporated in the detection techniques of most telescopes, including Hard X-ray telescopes. Instead The LAT detects these high-energy particles by incorporating a typical high energy physics particle detector setup, that includes a converter-tracker system fabricated of silicon and high-Z material layers and an electromagnetic calorimeter.

The converter-tracker is formed using 16 separate modules with 16 layers of tungsten paired with silicon scintillators sheets positioned immediately below. Figure 4-2 shows the arrangement of the converter/detector layers within the LAT tracker. The telescope takes advantage of the fact that γ rays do not reflect or refract and instead of direct detection, as can be done for even high-energy X-ray sources, uses the tungsten layers to convert the photon into an electron-positron, e^-e^+, pair through

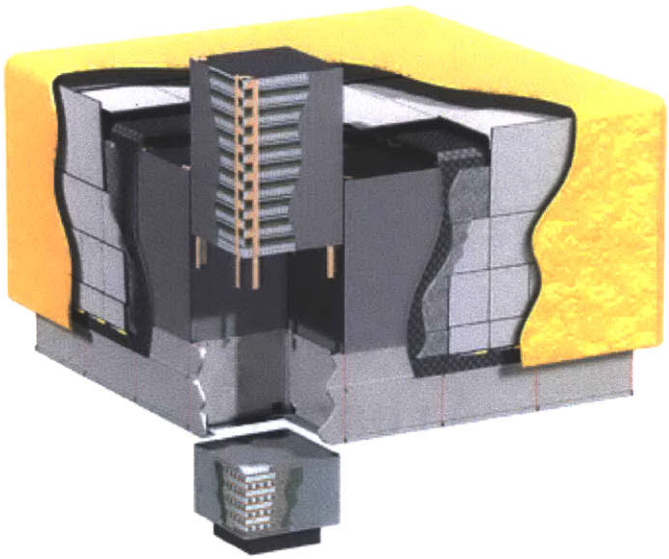

Figure 4-1: Diagram of the Large Area Telescope including the ACD layer (gold), the tungsten-silicon tracker (raised out of image), the electromagnetic calorimeter (lowered out of image), and DAQ attached at the bottom of the calorimeter [9]

weak interactions, that can be detected with high accuracy. In this way the tracker allows a precise determination of the direction of approach of incident particles as well as catalyzes their conversion so that it may be contained within the 0.72 m depth of the telescope [9]. Multiple scattering and bremsstrahlung production within the tracker has been shown to limit the the obtainable resolution, therefore optimal results require measurement immediately following the conversion [9].

After passing through the tracker, the resulting e^-e^+ pair pass into an electromagnetic calorimeter which is used to determine the energy of the incident particles, and reconstruct the energy of the incident photon. The reconstructed energy provides an important defining characteristic used in reconstructing the electromagnetic particle shower resulting from incident photons and determining important characteristics regarding the source and method of . The detection capability of the LAT is limited by the short depth of the telescope itself. As reported by Atwood et al. in 2009, the LAT calorimeter has a depth of 8.6 X_o on-axis for EM showers [6, 9]. Here X_o is the radiation length defined as the typical amount of matter needed for a gamma ray to convert into an e^-e^+ pair with units of g/cm^2. To overcome this depth issue,

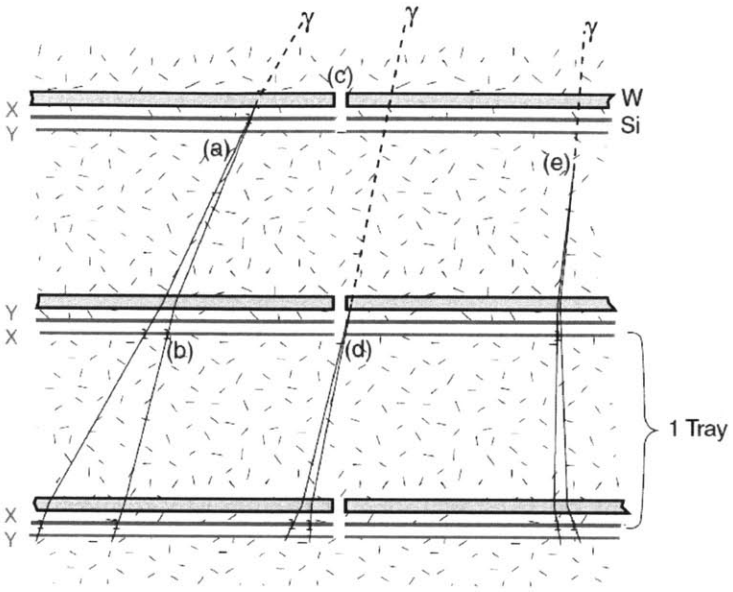

Figure 4-2: Image of tracker design. (a) shows the ideal conversion by the tungsten, W, layer and detection immediately following by the Si tracker. (b) segmentation allows detection of both particles resulting from conversion improving the point spread function and background rejection [9]

the longitudinal segmentation of the calorimeter enables energy measurements up to 1 TeV and also contributes significantly to background reduction [9].

Surrounding the LAT tracker and calorimeter layers is a segmented, 10 mm thick anti-coincidence detector (ACD) layer used to provide initial charged-particle background rejection. The ACD was designed to provide a minimum of 0.9997 efficiency [9]. This is achieved using scintillator tiles attached to wavelength shifting fibers embedded in the tiles coupled to two photomultiplier tubes. The entire apparatus is also covered in a low-mass micrometeoroid shield to protect the telescope from damage. The on board Data Acquisition System (DAQ) performs the initial filtering of the data before sending it to ground based servers [6, 7, 9]. This filtering returns information concerning the quality of each recorded event. The data used in this study was all categorized as P7SOURCE_V6, which represents the highest quality photon events. At times data was analyzed using the these events that were converted at the front of the machine which the DAQ distinguishes as P7SOURCE_V6:FRONT events [6].

To summarize, the Fermi Gamma-ray Space Telescope spacecraft is an excellent tool for studying γ-ray emission because of its improved angular resolution from other experiments, such as EGRET and ground based experiments, as well as its position in low Earth orbit. These studies include investigations into cosmic ray acceleration and high energy emission from supernova remnants [30]. The Large Area Telescope was designed to detect photons from radio to γ-ray energies, allowing for broadband analysis of SNR emission spectra and also morphology. The processes needed to analyze LAT data is introduced in the next section. These steps and this instrument will allow a more complete understanding of Kes 41's spectrum and structure and will ultimately shed light on the existence of cosmic ray acceleration therein.

Chapter 5

Methods

Since August 8, 2008, the FGST LAT has been in obit, collecting data for the entire night sky every three hours in what is called survey mode. This collection is more or less a passive process where particle events are collected for an enormous range of energy. The LAT's onboard Data Acquisition System (DAQ) performs initial filtering of recorded events based on several parameters in an attempt to establish that recorded events are of cosmic origin and not false positives [6, 9]. This restricts the total amount of information retained and passed on to the space craft's data servers where additional filtering is conducted, further restricting the data set to events corresponding to cosmic phenomena.

The data set used in this analysis was collected over the entire runtime of the experiment, ranging from the start of data collection on August 8, 2008, MET = 239557417, to March 8, 2013, MET = 384612418, where MET stands for mission elapsed time. Analysis of LAT data is typically carried out by utilizing the Fermi Science Tools, a command line and python based software toolbox developed specifically to aid in Fermi LAT analysis. Figure 5-1 shows the organization of this tool kit. We can see that this is a complex framework which includes data selection tools and a large classification of tools used for likelihood analysis. These two categories will be very important to the data analysis presented in this paper and will be further explained in the next section. This analysis will also use the *gtbin* tool as part of the analysis on Kes 41's γ-ray morphology. The following discussion will follow the

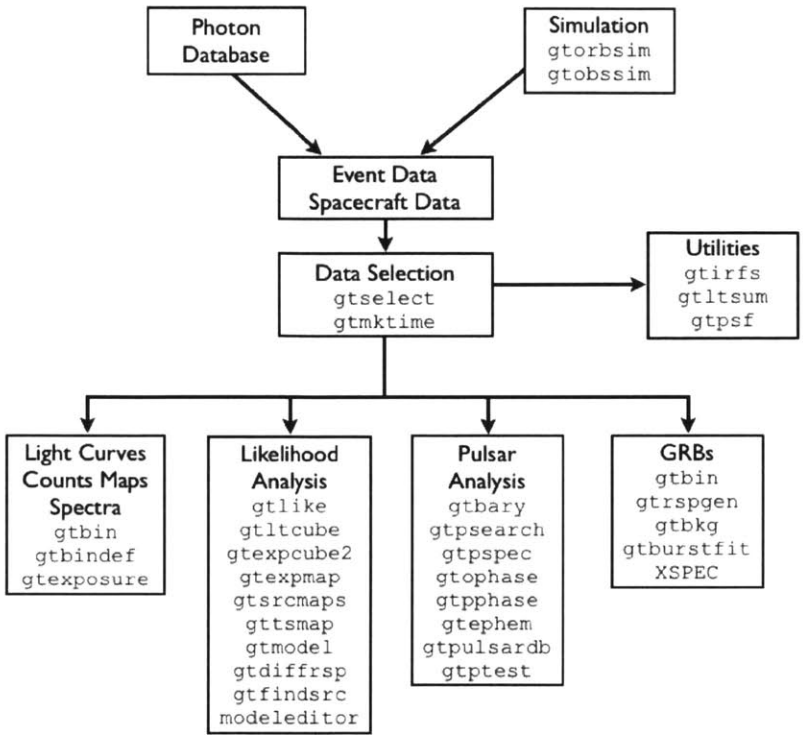

Figure 5-1: Diagram of the analysis tools used for Fermi LAT data analysis [30]

descriptions given by the Fermi Science Tool online Reference Manuel and Cicerone Documentation, online guides produced and maintained by the NASA Goddard Space Flight Center for Fermi LAT analysis.

5.1 Event Selection

The first step to LAT data analysis is downloading data sets from the LAT data server, shown in Figure 5-1 as the Photon Database. This requires the first instance of researcher-inputted restrictions on the data, referred also as cuts. These cuts include establishing the energy range, time of detection and reconstructed location of the events to be used in analysis. The location restriction is done by selecting a center coordinate in right ascension and declination for which the server then provides a full data sets that include this point. This allows focus on a point source as well as extended objects such as supernova remnants through further selection steps. The data sets produced by the data server include several photon data sets corresponding

to different detection time intervals, as well as a spacecraft file containing important information regarding the operation of the LAT during the time range inputted.

Following the acquisition of data sets, we then apply further cuts to the data using the *gtselect* tool from the Fermi Science Tools toolbox. This tool allows an additional opportunity to restrict data sets in time and energy range, which is used during the spectral analysis part this work. Again we also input the coordinates of a selection cone that includes a cone center corresponding to that inputted to thte data server, which for Kes 41 is (RA, Dec) = (249.75, -45.983333), as well as a radius around this center for which data will be used. For this analysis, selection radius was set to 20 degrees. We also may restrict events based on what depth within the LAT tracker the incident photons were converted. For the analysis on Kes 41's morphology, events recorded in the 'Front' of the detector, the first 8 scintillator/converter layers, were used exclusively because this ensures a better quality photon data set by helping to eliminate false positives caused by multiple scattering deeper in the tracker. It also allows more accurate direction reconstruction due to the longer recorded track resulting in a better overall angular resolution. Finally, we set a maximum reconstructed zenith angle allowed in the data set. This prevents the inclusion of events that could be created by terrestrial photon emission due to cosmic ray interactions with the Earth's atmosphere. A common chosen value, and the one used during this work, is 100^o, where the zenith angle is defined as the angle from the LAT's line of sight at the moment of detection to the reconstructed direction of the photon.

Because of the complexity of the FGST and its ability to be remotely pointed and boosted to maintain its orbit etcetera, there are times when events recorded by the LAT correspond to time intervals when some type of adjustment to the telescope was being made. This adds a systematic error to the affected events and can greatly affect the results of the entire analysis. In order to restrict analyzed photon events to those that occurred at times of optimal telescope performance, another Fermi Science Tool, *gtmktime*, is used to establish "good time intervals" (GTI). These GTI's are established through the incorporation of the spacecraft file which contains information including the LAT live time, the pointing of the telescope, the spacecraft altitude,

and other characteristics regarding the state of both the LAT and the FGST at the time of each event detection. Once these intervals are set, the tool produces a final data set containing all events that occurred within the GTI's.

5.2 Adjust for Livetime and Exposure Systematics

Just as there are GTI's for proper data collection, there are systematic effects of the space craft that skew the efficiency of data collection including livetime and the amount of time the telescope's line of sight is pointing in a particular direction. Livetime refers to the time the telescope is actively taking data. This can vary quite a bit as Figure 5-2 demonstrates. This plot was created using events of reconstructed

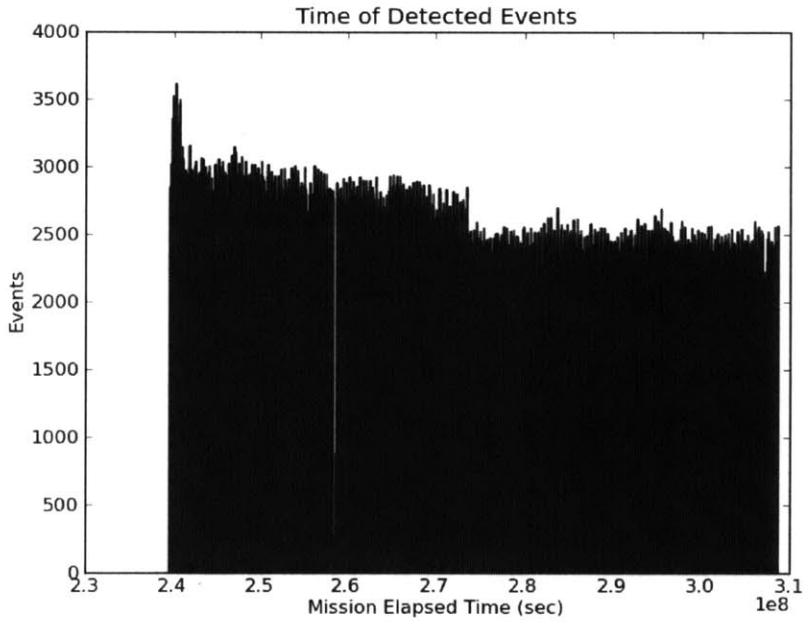

Figure 5-2: Sample distribution of recorded 1TeV events for the first 800 days of LAT data taking, [24]

energy $\gtrsim$ 1TeV and cuts that restricted analyzed events to those of cosmic ray proton detection [24]. This plot of counts received for bins of time, despite the different energy scale and applied cuts, still gives a clear idea of moments when the LAT recorded events and did not. The fluctuations in the height of each bin includes a

great deal of physics but many of the fluctuations, especially the particularly large drops, correspond to moments when the LAT was simply not recording data.

Therefore, proper analysis of Fermi LAT data requires accounting for the livetime of the telescope. This is done by creating a livetime cube using the GTI data produced by the *gtmktime* tool, and the spacecraft file. The livetime can be viewed as a function of the three dimensional space comprising both the sky position, in right ascension and declination, and the inclination angle. We can define the detector's line of sight as the z-axis of the apparatus. The pointing of the telescope affects the data by varying the inclination, the "off-axis angle", of reconstructed events. The tool which creates the cube is called *gtltcube* and it operates by extracting the spacecraft pointing history from the spacecraft file along with the time range and GTI selections established during the *gtmktime* step. The tool creates a record of the livetime spent at each position in the sky for the entire sky to be used later in the likelihood analysis steps.

To put this livetime information into a form that can be used during future analysis, we need to create an exposure map. This map calculates the overall exposure of the telescope for different energies at different inclination angle. This calculation consists of essentially integrating the total response of the LAT at different energy, time and position. This integral therefore includes the effective area, the energy dispersion times, and the point spread function of the LAT for the entire spatial and energy range of interest. This is done using the tool *gtexpmap*. Instead of creating a map that covers the entire sky, this tool only does so for a set region of interest (ROI) around the chosen central point.

During the data selection step, a source region radius was set for which data was retained. The ROI is a similar restriction on the data but because the LAT point spread function is broad at low energies, this cube should be made for a radius 10 degrees larger than that set in the source region. The term broad refers to the fact that $\sim$ 68% of counts lie within 3.5 degrees of the source at energies on the order of 100 MeV. This is important to this analysis because the energy range set was from 200MeV - 200GeV. The LAT point spread function goes as roughly the energy, $E^{-0.8}$. Therefore for energies, $>$ 1GeV, the ROI only needs to be a few degrees larger than

the source region. The tool also requires a spatial and energy gridding input which we set as half-degree pixels for a 30 degree radius, and ten logarithmically spaced energy bins used to divide the entire energy range.

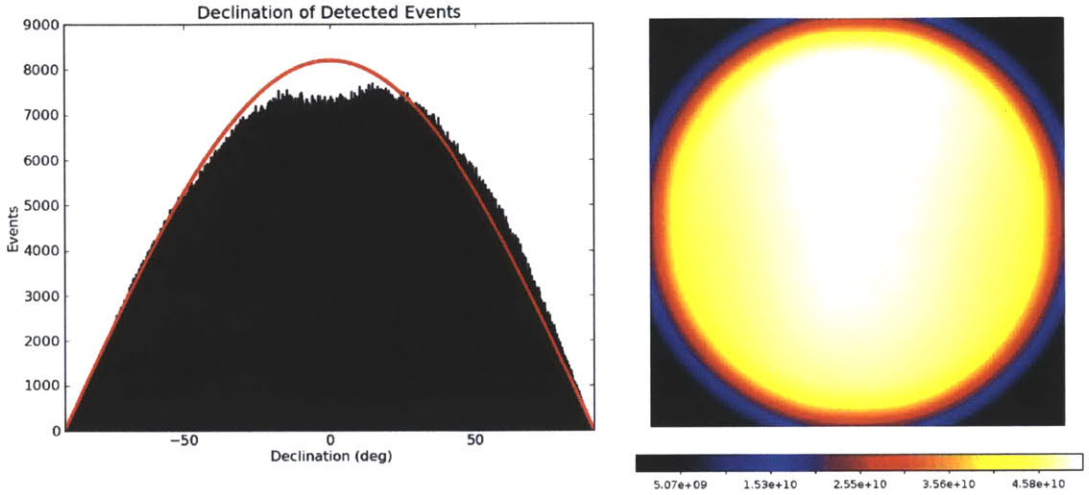

(a) Plot indicating a deviation between the recorded distribution of declination for events and the theorized cosine curve in red [24]

(b) Smoothed plot displaying the small but measurable differences in LAT detection at different Right Ascension and Declination

Figure 5-3: Evidence of the systematic effects on LAT data taking

Figure 5-3a shows the effects of systematic effects on data taking. Specifically, it shows the distribution of counts over bins in declination created for the same analysis used to produce Figure 5-2. The red line is the theoretical model for the distribution of events per reconstructed declination, a simple cosine curve normalized to the total number of events. There is an obvious discrepancy between this model and actual distribution. This is due again in part to real physics but it is mainly a result of systematic effects of the spacecraft that need to be accounted for. Figure 5-3b shows example of an exposure map created by taking these steps.

5.3 Likelihood Analysis

The likelihood is the probability calculated for obtaining the value recorded in experimental data in reference to the predictions of a theoretical model. In this case,

the input model is the distribution of gamma-ray sources on the sky as the LAT would measure is including their intensity and spectra. Obviously this requires that the response of the LAT to the incident flux is sufficiently well understood. This knowledge will ensure accurate mapping of the input model to the data, the recorded events. Other statistical methods typically use the maximization of a χ^2 statistic to measure this probability but because the LAT data is simply too sparse, this cannot be done for LAT analysis. Therefore, data analysis requires a full Poisson likelihood optimization for model parameter estimation.

The LAT data is automatically organized into bins characterized many variables of many different type and purpose including position, energy, conversion depth, time of detection, and many more. In this analysis the likelihood L will therefore be defined as the product of the probabilities of observing the detected counts in each bin. We can assume that the expected number of counts in the i-th bin is n_i. This number however, is predicted differently by the different models making it dependent on the source model chosen for the analysis. The probability of detecting m_i photons in this bin is simply given by $p_i = n_i^{m_i} e^{-n_i}/m_i!$. The likelihood L is simply the product of p_i calculated for all i bins. This product also factors into the product of the $n_i^{m_i}/m_i!$ values, that depends on both the values recorded for m_i by the detector and the product of the e^{-n_i} terms. The product of the e^{-n_i} terms for all i bins is equal to the exponential of the n_i terms minus their sum. The sum of n_i is simply the total number of predicted counts, N_p that the source model determined should have been detected by the LAT.

Therefore, the likelihood L can be factored into e^{-N_p}, a function of the source model alone, and the product of the individual $n_i^{m_i}/m_i!$ terms, which is a function of both the source model and the data. This is given by,

$$L = e^{-N_p} \prod_i \frac{n_i^{m_i}}{m_i!} \tag{5.1}$$

This likelihood has been written with finite size bins, and m_i that may take values greater than 1. This is the basis of binned likelihood analysis. However, the statistical

analysis in this work will be conducted using an unbinned approach because binning actually destroys information including the precise values of quantities that describe individual events. With binned analysis there the number of bins, effectively the bin size has a large effect on the accuracy of the calculations. Basically smaller bins result in a more accurate likelihood measurement Unbinned analysis takes this to the extreme by letting the bin sizes get infinitesimally small. This means that n_i can only equal 0 or 1. This makes the likelihood the product of e^{-N_p}, and m_i where i is now the index over the counts instead of bins.

$$L = e^{-Np} \prod_i n_i \tag{5.2}$$

Since n_i is calculated using the precise values for each count, and not an average over a finite size bin, this unbinned likelihood is the most accurate method for parameter prediction. For a small number of counts the unbinned likelihood can be calculated rapidly, but as the number of counts increases the time to calculate the likelihood becomes the limiting factor.

Fitting involves finding the set of parameters that maximizes the likelihood using a given model. Since the likelihood is a non-linear function of the parameters, algorithms for maximizing non-linear functions can be used. The maximum is found by iteratively calculating the function for different sets of trial parameters; by estimating derivatives of the function with respect to the parameters, the algorithms choose new trial parameters that are progressively closer to the set that maximizes the function. The function is calculated for new sets of trial parameters until the change in the function value between iterations is sufficiently small or the number of iterations reaches a maximum value. While iterating, these algorithms map out the dependence of the function on the parameters, particularly near the function's maximum. The uncertainties on the best fit parameters are related to this dependence. This process requires the implementation of a specific optimizer tool or algorithm.

Generally speaking, a reasonable strategy is to run the likelihood analysis tool *gtlike* with the DRMNFB optimizer until convergence, then running the tool using

the NEWMINUIT optimizer, using the inputted best fit parameter values produced during the first run to calculate the errors on the parameter values more accurately. This sequence makes sense because the DRMNFB optimizer is efficient at finding the maximum likelihood but also approximates the parameter dependence near the maximum. Because of this, the uncertainties provided may not be reliable. Conversely, the NEWMINUIT optimizer is considered a conservative optimizer, developed by CERN for high energy physics data analysis, that converges more slowly than other optimizer algorithms. Because of this slowness, the optimizer can exhaust the number of permitted iterations before convergence, resulting in an unreliable maximum likelihood. However, NEWMINUIT actually maps the parameter space near the likelihood maximum better than DRMNFB, providing more reliable uncertainty estimates. The *gtlike* tool requires the input of the GTI file, the exposure map, livetime cube, optimizer, as well as a theoretical model to be used for the optimization process.

5.4 Model Setting

Establishing the appropriate model for extended sources, such as supernova, requires modeling local gamma-ray sources within the ROI set during the *gtexpmap* step as well as several sources of background flux. This is necessary because these background sources effectively obscure the emission from the source cone of interest, greatly effecting its statistical significance. The *gtlike* tool requires the input of a source library which lists the coordinates of γ-ray sources nearby the source of interest and also the appropriate model to approximate its flux. These models include various power law models for extended objects and diffuse sources, exponential cutoff functions, gaussians and also the choice of modeling a source as having a constant valued flux.

To model the background sources, this analysis includes both the model of the galactic diffuse emission background and the extragalactic isotropic diffuse emission background, which includes the residual cosmic ray background. These are approximated using models developed for LAT Likelihood analysis, gal_2year7v6_v0.fits for the galactic emission and iso_p7v6source.txt to model the extragalactic background.

THIS PAGE INTENTIONALLY LEFT BLANK

Chapter 6

Analysis of Results

6.1 Spatial Analysis and Morphology

The first steps of the study of Kes 41's morphology used the *gtbin* tool to create a counts map from the data set resulting from the *gtselect* process. The tool simply appropriates the number of counts recorded at specific points in Right Ascension and Declination into bins of specific angular size. In this analysis we used bins of 0.01 degree width. Figure 6-1a shows the result of this step, displaying event counts for a region around the center coordinate with a 10^{o}. This map has also been smoothed using the ds9 imaging software. Also included are the positions of surrounding γ-ray sources lying along the galactic plane. Figure 6-1b shows the zoomed in image. Here we can see the proximity of the peaks in γ-ray events with the radio contours and the OH-maser emission, shown by the black +. However, without a statistical measure, we cannot yet make definitive claims regarding Kes 41's γ-ray morphology.

To do this, the next step of the spatial analysis used likelihood analysis to measure the significance of the recorded number of event counts over a set spatial region surrounding Kes 41. Instead of using *gtlike*, where the parameter values were maximized according to an energy range, we used the tool *gttsmap* which conducts the full likelihood analysis, previously described in Section 5.3, for many different points within the chosen region. Basically, this tool conducts multiple *gtlike* optimizations for the entire range in energy, 200MeV- 204.8GeV, for a spatial grid of points at dif-

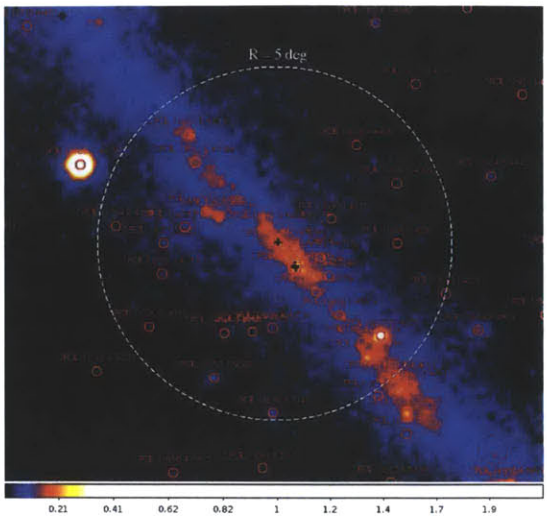

(a) Counts map of Kes 41 using 0.01 degree bins including a region file that indicates position of neighboring γ-ray sources (red circles)

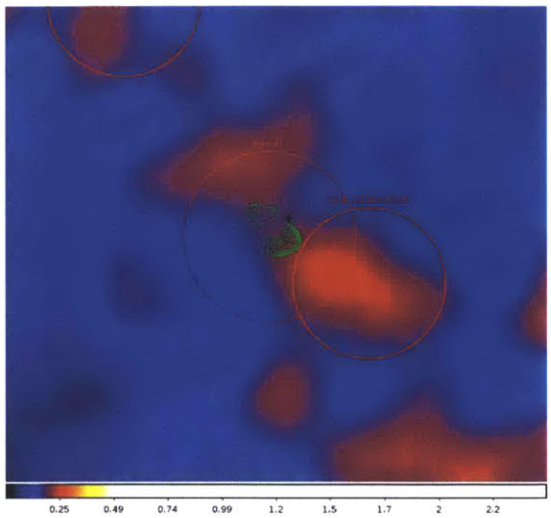

(b) Zoomed in counts map of γ-ray emission. Superimposed are the MOST 843 MHz radio contours and the location of OH-Maser emission (black +)

Figure 6-1: Smoothed counts maps produced using the selected data for a 10 degree radius around the center of Kes 41 (RA, Dec) = (249.75, -45.983333), with 0.01 degree bin width. Also included are the locations of other point and extended γ-ray sources along the galactic plane. OH-Maser emission and 843 MHz Kes 41 radio contours are also plotted and are especially noticeable in the zoomed in map [25, 31]

ferent RA and Dec coordinates inside the region instead one run covering the whole region. This makes the process quite time consuming so this analysis was restricted to using a region of 0.5 degree radius, using 0.02 degree bin widths. This region is established by inputting the center of the region of interest and selecting a number of spatial bins of a specific size. Therefore the input specified 50 bins in both latitude and longitude, of 0.02 degree widths. After inputting these values, the tool essentially moved a putative point source through the grid of bins, maximizing the test statistic, TS = -log(Likelihood), value at each point. The value is then recorded and plotted at the coordinate on the outputted TS-map.

The result of this analysis can be seen in Figure 6-2. Here we see a map showing the probability of the existence of a source at each spatial point, based on the recorded flux at each point for the total energy range. The points on the map where the color corresponds to a test statistic > 25 indicates a 5σ detection, which we claim as statistically significant emission. This occurs over the region contained within

the superimposed radio contours. This suggests a centrally bright γ-ray morphology. Looking closely, it appears that the largest TS values have been recorded toward the lower right of the radio contours, corresponding perhaps to the lower peak of radio emission seen in the radio image, Figure 3-1b [25, 31].

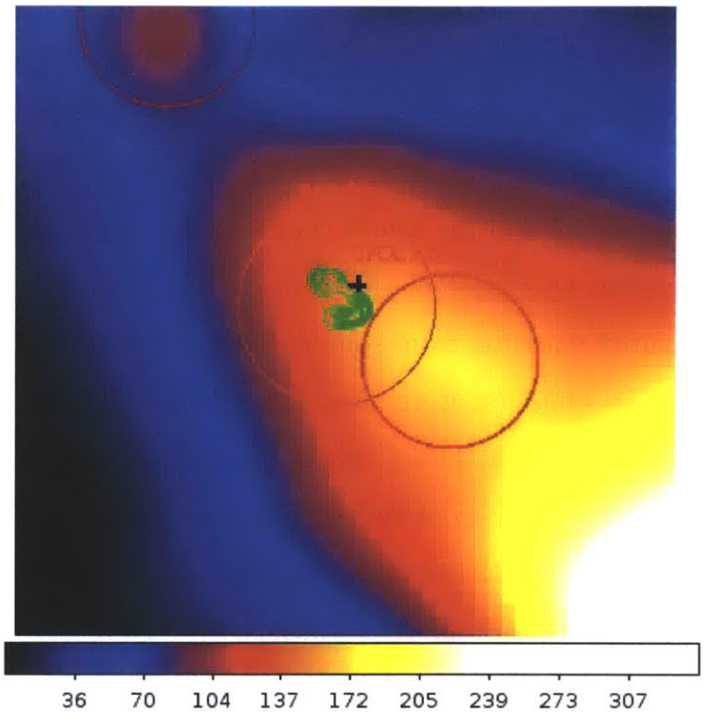

Figure 6-2: Test Statistic map of γ-ray emission from Kes-41 with 843 MHz radio contours (green) overlayed and the OH-maser emission located in the upper right of the image (black +) . Includes the position of γ-ray sources given in red [25, 31, 32]

Also plotted is the point of OH-maser emission which is also contained within the region of significant γ-ray emission. This proximity may be evidence for the interaction of the SNR ejecta and a nearby molecular cloud. If this is true then it may also be evidence of the acceleration of hadronic cosmic rays within the SNR. Comparing this map with that of the X-ray emission, Figure 3-2, discussed in Section 3.2, we can see that both spectra appear centrally bright, with the strongest emission coming from the location of the peak radio emission. The similarity between these two high energy spectra provides further support of the significance of the γ-ray emission, and helps with the interpretation of its morphology. The close proximity of the maximum TS values to the point of OH-maser emission also may provide evidence of cosmic ray

acceleration within Kes 41. The image also begs a higher angular resolution which may allow the detection of subtleties in the spatial distribution.

6.2 Spectral Analysis

The spectral analysis was conducted by using an initial source library including all gamma-ray sources within a 25 degree radius of the Kes 41 center, including a modeled source for Kes 41 itself, with its emission defined by a power law model. For those point sources within 5 degrees of the center coordinates, the parameters were allowed to adjust while the sources outside of this range were not allowed to change. This is because the measured emission from sources within 5 degrees of Kes 41 may well be influenced by either emission from Kes 41 or interaction with material in the remnant itself. Therefore the fit being run using *gtlike* should adjust these values during its optimization in order to arrive at the most physically appropriate values. Following the recipe given in Section 5.3, the data was fitted using the DRMNFB optimizer first. The xml file produced following this fitting was then used as the source model for a second *gtlike* run using the NEWMINUIT optimizer. During this second run, only the background sources, described in Section 5.4, and the Kes 41 source were allowed to adjust their parameter values to the fit. This restricts the NEWMINUIT optimizer to focus on the parameter values set during the previous run, allowing a better calculation of these parameter's errors, and reducing the time taken to accomplish the fit.

In order to get a full understanding of the emission spectrum of Kes 41, the xml file produced following these fitting runs was then used as the inputted source file for a binned analysis. The only change was that the Kes 41 source emission was modeled by a constant value instead of a power law. The data range was cut into ten, logarithmically spaced, bins in energy and the analysis steps taken for the entire data set were then repeated for each of the ten individual data sets. This required rerunning the *gtselect* step, recalculating the GTIs, and making new exposure maps for each energy range. The livetime cube did not have to be remade because it was

initially made for the entire sky. Following each *gtlike* run, using the NEWMINUIT optimization, the outputted xml files recorded the best fit values of Kes 41's flux for each energy range. These values were then converted into particle flux using an outputted scale factor.

Interval (GeV)	Flux (ergs/cm^2/s)	Error	Log Flux	TS Values
0.2-0.4	5.61×10^{-19}	2.56×10^{-16}	-18.25	1.8×10^{-5}
0.4-0.8	8.26×10^{-13}	4.67×10^{-13}	-12.08	0.134
0.8-1.6	2.24×10^{-11}	2.32×10^{-12}	-10.65	112.9
1.6-3.2	2.11×10^{-11}	2.21×10^{-12}	-10.68	127.4
3.2-6.4	1.09×10^{-11}	1.94×10^{-12}	-10.96	49.13
6.4-12.8	3.27×10^{-12}	1.59×10^{-12}	-11.48	6.401
12.8 - 25.6	1.33×10^{-12}	1.81×10^{-12}	-11.88	0.655
25.6 - 51.2	1.43×10^{-12}	2.76×10^{-12}	-11.84	0.314
51.2 - 102.4	1.30×10^{-18}	1.85×10^{-15}	-17.89	8.1×10^{-7}
102.4 - 204.8	3.36×10^{-18}	7.96×10^{-16}	-17.47	2.0×10^{-6}

Table 6.1: Table summarizing the results of *gtlike* optimization for 200MeV - 204.8GeV emission including TS values

Flux is typically measured in terms of energy flux in units of ergs/cm^2/s. So the scaled flux values were then converted into energy flux by multiplying them by the logarithmic energy bin center, E_c^2, and finally by the conversion factor to transform from units of MeV to ergs, 1.602×10^{-6}. The resulting values are included in Table 6.1, along with the corresponding maximum TS values found during the *gtlike* optimization.

From the table we can see that there is a large variation in the order of magnitude of several of these values, as well as the corresponding errors. This indicates essentially a poor fit by the optimizer which is made more apparent by correspondingly low TS values. For energy ranges with a TS < 25, we can say there is a less than 5σ significance of the recorded flux.Therefore we have unreliable data for those ranges and need another measure to understand the flux. In this analysis three regions had TS values > 25, including the energy range from 0.8-6.4GeV. To gain another estimate of the flux from those intervals with less than 5σ detection, upper limit values of the flux were calculated using the python based likelihood analysis tool, pyLikelihood.

The results of this limit setting can be seen in Table 6.2, reported alongside the flux values from the three significant energy intervals. From this table we see much closer values for the flux and the upper limits than before.

Interval (GeV)	Upper Limit	Flux (ergs/cm^2/s)	Error	Log Flux
0.2-0.4	4.52×10^{-11}			-10.34
0.4-0.8	2.81×10^{-11}			-10.55
0.8-1.6		2.24×10^{-11}	2.32×10^{-12}	-10.65
1.6-3.2		2.11×10^{-11}	2.21×10^{-12}	-10.68
3.2-6.4		1.09×10^{-11}	1.94×10^{-12}	-10.96
6.4-12.8	6.17×10^{-12}			-11.21
12.8 - 25.6	4.88×10^{-12}			-11.31
25.6 - 51.2	6.89×10^{-12}			-11.16
51.2 - 102.4	3.95×10^{-12}			-11.40
102.4 - 204.8	4.43×10^{-12}			-11.35

Table 6.2: Table summarizing the results of *gtlike* optimization for 5σ flux values and upper limit setting on the flux (ergs/cm^2/s) corresponding to energy intervals with TS < 25. The Log Flux column includes logarithmic of either value as they apply to the corresponding energy interval

Figure 6-3 shows these final flux and upper limit values plotted over the entire analyzed energy range, 200MeV-204.8GeV. This can be interpreted as the plot of the high energy non-thermal spectrum of Kes 41. Included in the figure is also fit to the three flux points using a power-law function given by,

$$E^2\frac{dN_i}{dE} = c\left(\frac{E}{E_{0_i}}\right)^{-\Gamma} E^2 \tag{6.1}$$

where E_{0_i} is the logarithmic center of the i-th energy interval and Γ is called the spectral density. The fit resulted in parameter calculations of $c = 1 \times 10^{-9}$, and $\Gamma = 0.521$. From this plot we can see that the power law fit approximates the data quite well including the upper limit calculations shown as down-ward pointing triangles. This close modeling indicates that we have obtained a predictable SNR high energy emission spectrum, that agrees with the theorized functional form for γ-ray emission.

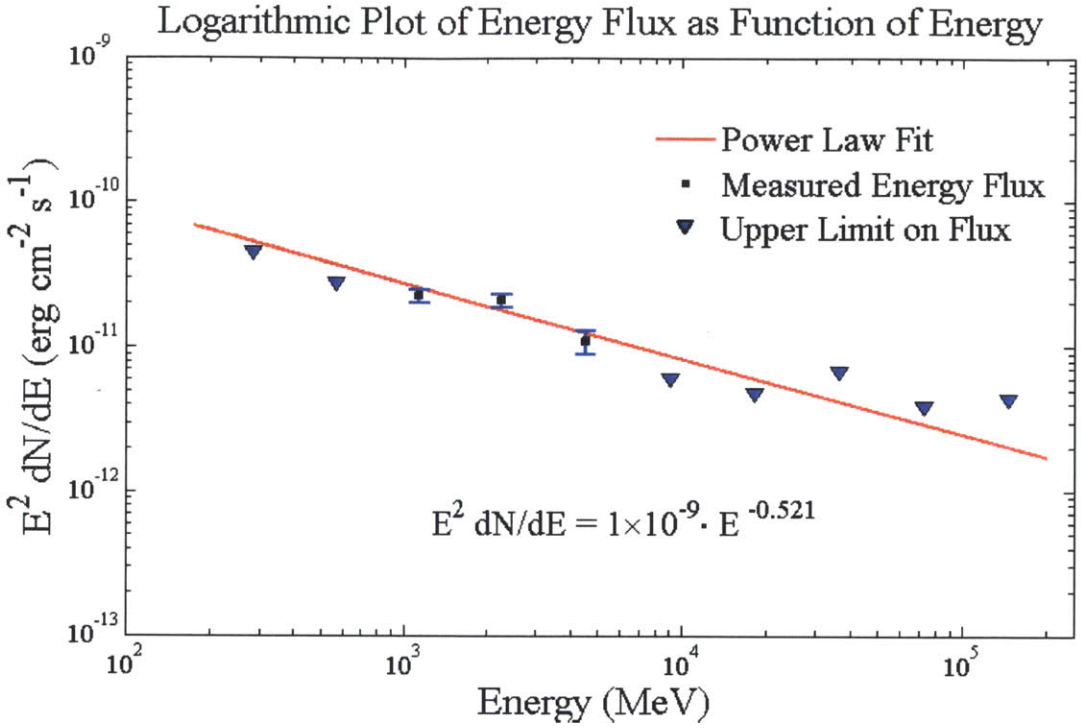

Figure 6-3: Logarithmic plot of the high energy γ-ray spectrum for Kes 41 emission. The data points (black) represent flux values produced by likelihood maximization process for 5σ detections, TS > 25. The triangles correspond to calculated upper limits set on the energy flux for energy ranges with TS < 25. Included also is a power law fit to the TS > 25 data (red line)

6.3 Luminosity Approximation

The parameters resulting from a fit of the three significant dN/dE flux values from Table 6.1 can be used to calculate an approximate value of the overall γ-ray luminosity, L_γ of Kes 41 for the entire energy range. This is simply an approximation because the fit function only used the three significant flux values and therefore cannot have a low enough χ^2 value to rigorously validate the fit. Conducting this fit with the same power law functional form gave parameter estimations of $c = 6\times10^{-4}$, and $\Gamma = 2.521$. Taking an integral of the resulting dN/dE equation over the full energy range gives an estimation of the total detected energy flux, N_E, from Kes 41. This is done by taking an integral of Equation (6.1), multiplied by the energy, over the full energy

range, which may be written as,

$$N_E = \int_{E_{min}}^{E_{max}} \frac{dN}{dE}\, E\, dE \tag{6.2}$$

Where dN/dE is given by the power law functional form using the parameters produced during fitting. Following through with the integration and converting to ergs using the value stated previously results in an estimate of $N_E = 1.0217 \times 10^{-11}$ erg/cm^2/s. From here we can quickly calculate the approximate luminosity using the following equation,

$$L_\gamma = N_E\, 4\pi D^2, \tag{6.3}$$

where the $4\pi D^2$ value corresponds to the solid angle of a distant source. D in this case is the distance to Kes 41 which has been measured previously as $\sim$ 12.6kpc [25]. This then results in a total γ-ray luminosity, $L_\gamma = 1.94 \times 10^{35}$ erg/s.

Chapter 7

Discussion and Conclusions

In this thesis, the γ-ray spectrum of an SNR, a theorized source of cosmic ray diffusive shock acceleration, was analyzed using data recorded by the FGST LAT over the entire mission life of the telescope, from August 4, 2008 through March 8, 2013. The energy range used in this analysis was taken for 200MeV - 204.8GeV, corresponding to high energy, γ-ray emission from non-thermal emission processes including π^0-decay due to hadronic cosmic ray acceleration. This π^0-decay is theorized to result from proton-proton collisions which are made more probable by interaction with proximate molecular clouds due to a denser concentration of particles. SNR-MC interactions constrain the source of γ-ray to the π^0-decay channel. The SNR Kes 41 was chosen as the γ-ray source of interest because of its proximity to a source of OH-maser emission, wihich is indicative of the presence of an MC [18, 22, 25].

Using the Fermi Science Tools data analysis toolkit, the γ-ray morphology of Kes 41 was mapped for a 20 degree radius surrounding the center of the remnant. Then using likelihood analysis the statistical significance, recorded as a test statistic value, was calculated for bins over a 0.5 degree radius region. This γ-ray morphology was determined to be a $> 5\sigma$ detection over the entire region outlined by the previously measured radio contours, and resembled the distribution of X-ray emission relatively closely despite a lower angular resolution [18, 25]. The closeness of these emission spectra supports the notion that this γ-ray emission is due to emission processes from Kes 41. Also, the proximity of this emission to the observed OH-maser emission

reinforces that this emission is likely due to π^0-decay, resulting from shock accelerated protons.

Likelihood analysis was also used to calculate the parameter values that maximized the probability of the occurrence of the received event counts, based on a theoretical model of local γ-ray sources. These values were then used to calculate the energy flux for logarithmically spaced energy bins to produce the γ-ray spectrum for Kes 41, Figure 6-3. For values that lacked the appropriate statistical significance, experimental energy flux values were replaced by upper limits again calculated through a likelihood analysis process. Then a typical model of γ-ray emission was fit to the three values of significant flux, from which was derived a functional form for the particle flux per energy dN/dE [12,22]. The parameters from the fitted model were then used to estimate the overall γ-ray luminosity of Kes 41 given by, $L_\gamma = 1.94 \times 10^{35}$. This luminosity is on the same order of magnitude as that measured for SNRs at similar distance reinforcing the spectral analysis reported in this paper [12, 13, 25].

An additional value measured was the number density, n, of particles within the molecular cloud that may be interacting with accelerated hadrons from Kes 41 to form γ-ray emission through π^0-decay. Using the energy flux calculated in Section 6.3, but taking 100MeV as the lower limit, and the distance, D, of Kes 41 from the observer, measured in [25], we can calculate this using the equation, $F_E = 4.4E - 7n\Theta E_{SN} D^{-2}$, where Θ is the fraction of the total supernova energy, E_{SN}, converted to cosmic ray energy [19]. E_{SN} is typically estimated to be on the order of 10^{51} erg and Θ will be given the rather high value of ~ 0.4. Carrying this equation through using these values, we arrive at an estimate of the number density, $n = 0.15$ particles/cm^{-3}. Compared to the density of the ISM, $n \sim 10^{-4}$ cm^{-3}, we can see that the value describes a region of much greater density than "empty" space. This density is also on the same order of magnitude of other similar measurements taken for MCs using other SNR γ-ray emission [19]. Though approximate, this value may support the hypothesis that Kes 41's is interacting with a proximate MC, thereby restricting the significant γ-ray emission observed in this analysis to the non-thermal π^0-decay channel, and perhaps indicating observational evidence of cosmic ray acceleration.

Bibliography

[1] Abbasi, R., Abdou, Y., Abu-Zayyad, T., et al. 2012, Astrophys. J. 746 3

[2] Abdo, A. A., Ackermann, M., Ajello, M., et al. 2012 Astrophys. J. v.10.4

[3] Abdo, A.A., Ackermann, M, et al. 2009 Astrophys. J.

[4] Abdo, A.A., Ackermann, M., et al. 2009 Astrophys. J. 706, pp. 1-6

[5] Abdo, A. A., Allen, B.T., Aune, T., et al. 2009 Astrophys. J. 698 pp. 2121-2130

[6] Ackermann, M., Ajello, M., Albert, A., et al. 2012, arxiv: 1206.1896v1

[7] Ackermann, B., Ajello, M., Atwood, W. B., et a.l 2011, arxiv: 1008.5119v3

[8] Amenormori, M., Bi, X. J., Chen, D., et al. 2009, J. Phys. Soc. Jpn. 78, pp. 88-91

[9] Atwood, W.B, Abdo, A. A., Ackermann, M., et al. 2009, Astrophys. J. 697 1071-1102

[10] Berezhko, E. G., Volk, H. 2006 Astron. Astrophys. 451

[11] Blandford, R., Eichler, D. 1987, Phys. Rep. 154 pp. 1-75

[12] Castro D., P. Slane, 2010 Astrophys. J. 717 372

[13] Caswell, J. L., Murray, J. D., Roger, R. S., Cole, D. J., Cooke, D. J. 1975, Astron. Astophys. 45, pp. 239-258

[14] S. Chandrasekhar, *Principles of stellar dynamics*, **659**, Courier Dover Publications (1942).

[15] Clark, G.W. 1957 Phys. Rev., 108, pp. 450-457

[16] Claussen, M. J. et al. 1997 Astrophy. J. 489 143

[17] Colin, P., Tridon, D.B., Britzger, D., et al. 2009, Proceedings of the 31st ICRC 2009

[18] Combi J. A., Albacete-Colomo J. F., Marti J. 2008. Astron. Astrophys. 448, pp. 25-28

[19] Drury L. O. Aharonian, F. A., Volk, H. J. 1994 Aston. Astrophys. 287, pp.959-971

[20] Fermi, E. Phys Rev., 75, 1169, 1949

[21] Guillian, G., Hosaka, J., Ishihara, K., et al. 2007, Phys. Rev., 75, 062003

[22] Hewitt J. W., Yusef-Zadeh, f., Wardle, M. 2009, Astrophys. J. 706

[23] Hess, V. F., Z. Phys. 13 (1912) 1084

[24] Joubert, T. 2012, Department of Energy SLAC SULI Final Paper

[25] Koralesky B., 1998 Astron J. 116 1323

[26] Lande J, et al. 2012 Astrophys. J. 756, pp. 22

[27] Reynolds S. P., Ann. Rev. of Aston. Astrophys. 46, pp. 89-126

[28] Rossi, B. 1948, Rev. Mod. Phys. 20 3

[29] Smith, P. D., Hughes, R.E., Winer, B. L., Wood, T.W. 2009, *Proceedings of the DPF-2009 Conference*

[30] Thompson, D.J., Baldini, L., Uchiyma, Y., 2011 Astropart. Phys.

[31] Large M.I., Mills B.Y., Little A.G., Crawford D.F. and Sutton J.M., 1981 Mon. Not. R. Astr. Soc., v194, pp 693-704

[32] Whiteoak, J. B. Z., Green, A. J., 1996, Astrophys. J.

[33] Vink J., 2012 *Supernova Remnants: the X-ray Perspective*, Astronomy and Astrophysics Reviews **20**, 1

[34] Zhang, J. L., Zhang, Yi., Cui, S. W., 2009, Proceedings of the 31st ICRC 2009